2017

Effect of inter- and intra-annual thermohaline variability on acoustic propagation

Chu, Peter C.; McDonald, Colleen M.; Kucukosmanoglu, Murat; Judono, Albert; Margolina, Tetyana; Fan, Chenwu

Chu, P.C., C.M. McDonald, M. Kucukosmamnoglu, A. Judono, T. Margolina, and C.W. Fan, 2017: Effect of inter- and intra-annual thermohaline variability on acoustic propagation. Proc. SPIE 10186, Ocean Sensing and Monitoring IX, 101860U (May 22, 2017); doi:10.1117/12.2258687

http://hdl.handle.net/10945/60915

Effect of inter- and intra-annual thermohaline variability on acoustic propagation

Peter C. Chu*, Colleen M. McDonald, Murat Kucukosmanoglu
Albert Judono, Tetyana Margolina, Chenwu Fan
Dept. of Oceanography, Naval Postgraduate School, 1 University Circle, Monterey, CA USA 93943

ABSTRACT

This paper is to answer the question "**How can inter- and intra-annual variability in the ocean be leveraged by the submarine Force?**" through quantifying inter- and intra-annual variability in (T, S) fields and in turn underwater acoustic characteristics such as transmission loss, signal excess, and range of detection. The Navy's Generalized Digital Environmental Model (GDEM) is the climatological monthly mean data and represents mean annual variability. An optimal spectral decomposition method is used to produce a synoptic monthly gridded (SMG) (T, S) dataset for the world oceans with $1^o \times 1^o$ horizontal resolution, 28 vertical levels (surface to 3,000 m depth), monthly time increment from January 1945 to December 2014 now available at the NOAA/NCEI website: http://data.nodc.noaa.gov/cgi-bin/iso?id=gov.noaa.nodc:0140938. The sound velocity decreases from 1945 to 1975 and increases afterwards due to global climate change. Effect of the inter- and intra-annual (T, S) variability on acoustic propagation in the Yellow Sea is investigated using a well-developed acoustic model (Bellhop) in frequencies from 3.5 kHz to 5 kHz with sound velocity profile (SVP) calculated from GDEM and SMG datasets, various bottom types (silty clay, fine sand, gravelly mud, sandy mud, and cobble or gravel) from the NAVOCEANO's High Frequency Environmental Algorithms (HFEVA), source and receiver depths. Acoustic propagation ranges are extended drastically due to the inter-annual variability in comparison with the climatological SVP (from GDEM). Submarines' vulnerability of detection as its depth varies and avoidance of short acoustic range due to inter-annual variability are also discussed.

Keywords: Synoptic monthly gridded (SMG) (T, S) data, Navy's Generalized Digital Environmental Model (GDEM), optimal spectral decomposition (OSD), sound speed profile, acoustic transmission, acoustic ray tracing, acoustic model BELLHOP), geo-acoustic parameter, sediment characteristics

1. INTRODUCTION

Temporal and spatial variability of the global temperature and salinity fields is important in climate change. In the past decade, several new coupled ocean-atmosphere phenomena regarding the temperature, such as the pseudo-El Nino (or sometimes called central Pacific El Nino) and the Indian Ocean Dipole (IOD), were discovered and recognized important in climate variability. The pseudo-El Nino is characterized by warmer sea surface temperature anomalies (SSTA) in the central equatorial Pacific and cooler SSTA in the eastern and western equatorial Pacific [1] [2], which is different from the El Nino with anomalous warming in eastern equatorial Pacific. El Nino and pseudo-El Nino have different teleconnection patterns. Taking the Atlantic Ocean as an example, less tropical storms and hurricanes occur during El Niño events; and more tropical storms and hurricanes appear during pseudo-El Nino events[2]. Chu [3] presented heat content tripole in world oceans and found the connection between interannual thermal variability in the tropical Pacific and Indian Ocean. The variability regarding salinity is also important since freshwater gaining from river run-off, surface freshwater flux [precipitation-evaporation (P-E)], and freshwater advection reduces upper layer salinity, stabilizes the water column, and in turn slows down the meridional overturning circulation (MOC).

*pcchu@nps.edu; phone 1 831 656 3688; fax 1 831 656 3686; http://faculty.nps.edu/pcchu/

Ocean Sensing and Monitoring IX, edited by Weilin (Will) Hou, Robert A. Arnone, Proc. of SPIE
Vol. 10186, 101860U · © 2017 SPIE · CCC code: 0277-786X/17/$18 · doi: 10.1117/12.2258687

Using regional data, Phillips and Wijffels [4] identified an average freshening of 0.2 psu extending from 100°E to Australia, 25°S to Indonesia and down to 180 m depth, for more than 3 years from 1999 to 2002. The observed freshening can be largely explained as a direct response to changes in the air-sea freshwater exchange. Boyer et al. [5] calculated linear trends of zonally averaged salinity anomalies from 1955–1959 through 1994–1998 from the World Ocean Database 2001 (WOD01) and identified freshening and salinization in ocean basins such as freshening in most of the Pacific with the exception of the subtropical South Pacific, deep freshening in the Atlantic subpolar gyre, shallow salinization in the Atlantic tropics and subtropics, and salinization in the Indian Ocean at all latitudes in the upper 150 meter layer, with a subsurface freshening between 40°S and the equator in the 250–1000 meter layer.

Up until now, detailed temporal and spatial variability of global temperature and salinity fields has not been investigated from the observational data. This is because ocean observational (T, S) data are irregularly distributed in time and space. To fill the gap, several synoptic monthly gridded (SMG) (T, S) datasets have been produced at the NPS Department of Oceanography [6] with a sufficient resolution in space (1°×1° in global oceans and 0.25°×0.25° in several regional seas) and in time (monthly increment) using the optimal spectral decomposition (OSD) method [7][8][9][10]. These datasets have undergone thorough quality control by NOAA/NCEI scientists. With SMG (T, S) data, impact of intra- and inter-annual (T, S) variability on acoustical transmission can be identified.

2. OPTIMAL SPECTRAL DECOMPOSITION

The optimal spectral decomposition (OSD) method [7][8][9][10] is used to produce the SMG-(*T*, *S*) datasets, which are distributed openly at the NOAA/NCEI website. The basic theory and methodology are presented in this section.

2.1. Basic concept

Let $\mathbf{r} = (x, y)$ be the horizontal coordinates and z the vertical coordinate. The horizontal position vector ($\mathbf{r}$) is represented by $\mathbf{r}_n$ ($n = 1, 2, \ldots, N$) at grid points and by $\mathbf{r}^{(m)}$ ($m = 1, 2, \ldots M$) at observational locations. Here, N is the total number of the grid points, and M is the total number of observational points. Gridded temperature and salinity can be ordered by grid point and by variable, forming a single vector $\boldsymbol{c} = (T, S)$ of length NP with N the total number of grid points and P the number of variables (Fig. 1). For example, the background field ($\mathbf{c}_b$) is on the grid points and represented

$$\mathbf{c}_b^T = \left[c_b(\mathbf{r}_1), c_b(\mathbf{r}_2), ..., c_b(\mathbf{r}_N)\right], \tag{1}$$

where the superscript '*T*' means transpose. The observation ($\mathbf{c}_o$) is on the observational points and represented by

$$\mathbf{c}_o^T = \left[c_o(\mathbf{r}^{(1)}), c_o(\mathbf{r}^{(2)}), ..., c_o(\mathbf{r}^{(M)})\right]. \tag{2}$$

The objective of ocean data analysis and assimilation is to obtain an analysis field ($\mathbf{c}_a$) on the grid points using background field ($\mathbf{c}_b$) and observational field ($\mathbf{c}_o$). Difference between data analysis and assimilation is due to the use of $\mathbf{c}_b$: data analysis if $\mathbf{c}_b$ taking climatological data, and data assimilation if $\mathbf{c}_b$ taking numerical model output at present and/or past time steps. The analysis error ($\boldsymbol{\varepsilon}_a$) and observational error ($\boldsymbol{\varepsilon}_o$) are defined by

$$\boldsymbol{\varepsilon}_a = \mathbf{c}_a - \mathbf{c}_t, \quad \boldsymbol{\varepsilon}_o \equiv \mathbf{H}^T\mathbf{c}_o - \mathbf{c}_t, \tag{3a}$$

which are evaluated at the **grid points**. Here, $\mathbf{H} = [h_{mn}]$ is the $M \times N$ linear observation operator matrix. The two errors are usually independent of each other,

$$\left\langle \boldsymbol{\varepsilon}_o^T \boldsymbol{\varepsilon}_a \right\rangle = 0, \quad \langle\ \rangle \equiv \frac{1}{N-1}\sum_{n=1}^{N}[\ ]. \tag{3b}$$

Minimization of the analysis error variance

$$E^2 = \left\langle \boldsymbol{\varepsilon}_a^T \boldsymbol{\varepsilon}_a \right\rangle \rightarrow \min \tag{4}$$

gives the optimal analysis field $\mathbf{c}_a$ for the "true" field $\mathbf{c}_t$.

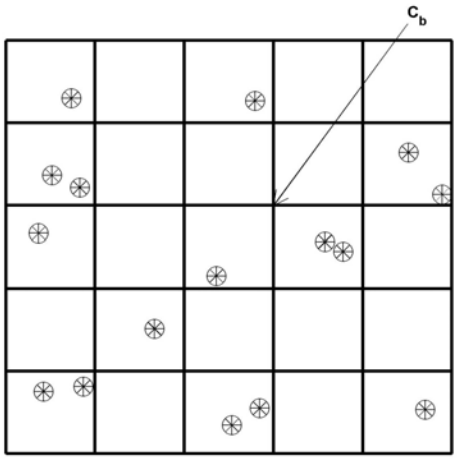

Fig. 1. Illustration of ocean data assimilation with $\boldsymbol{c}_b$ located at the grid points, and $\boldsymbol{c}_o$ located at the points '*'. The ocean data assimilation is to convert the innovation, $\mathbf{d} = \boldsymbol{c}_o - \mathbf{H}\boldsymbol{c}_b$, from the observational points to the grid points.

2.2. Two types of data assimilation

2.2.1. Weighted average

This type of methods is to blend $\mathbf{c}_b$ (at the grid points $\mathbf{r}_n$) with observational data ($\mathbf{c}_o$) (at observational points $\mathbf{r}^{(m)}$) into the assimilated (or analysis) field ($\boldsymbol{c}_a$) at the grid points $\mathbf{r}_n$,

$$\mathbf{c}_a = \mathbf{c}_b + \mathbf{W}\mathbf{d} \tag{5}$$

to represent the (unknown) "truth" $\mathbf{c}_t$ with an analysis error ($\boldsymbol{\varepsilon}_a$) and an observational error ($\boldsymbol{\varepsilon}_o$) given by (3a). Here, $\mathbf{W}= [w_{nm}]$, is the $N\times M$ weight matrix interpolating the innovation $\mathbf{d}$ into the grid points $\mathbf{r}_n$ (Fig. 1). Various minimization procedures give different weight matrices such as

$$\mathbf{W} = \mathbf{B}\mathbf{H}^T(\mathbf{H}\mathbf{B}\mathbf{H}^T + \mathbf{R})^{-1} \tag{6}$$

for optimal interpolation and Kalman filter and

$$\mathbf{W} = (\mathbf{B}^{-1} + \mathbf{H}^T\mathbf{R}^{-1}\mathbf{H})^{-1}\mathbf{H}^T\mathbf{R}^{-1} \tag{7}$$

for variational method. Here, $\mathbf{B}$ and $\mathbf{R}$ are the background and observational error covariance matrices. This type of methods requires ($\mathbf{B}$, $\mathbf{R}$) matrices being be given as *a priori* in order to determine the weight matrix $\mathbf{W}$.

2.2.2. Optimal spectral decomposition (OSD)

This type of methods is to avoid the use of background error covariance matrix ($\mathbf{B}$). Existence of a lateral boundary (Γ) for an ocean domain (Ω) provides a great opportunity to use a spectral method in ocean data analysis and assimilation through decomposing the variable anomaly at the grid points $[c(\mathbf{r}_n) - c_b(\mathbf{r}_n)]$ into the spectral form [9],

$$c_a(\mathbf{r}_n) - c_b(\mathbf{r}_n) = s_K(\mathbf{r}_n), \quad s_K(\mathbf{r}_n) \equiv \sum_{k=1}^{K} a_k \, \phi_k(\mathbf{r}_n), \tag{8}$$

where $\{\phi_k\}$ are basis functions; K is the mode truncation, which is determined using the steep-descending method [9]. The eigenvectors of the Laplace operator with the same lateral boundary condition of ($c - c_b$) can be used as the basis functions $\{\phi_k\}$. The $K \times N$ basis function matrix $\mathbf{\Phi}$ is calculated by

$$\mathbf{\Phi} = \{\phi_{kn}\} = \begin{bmatrix} \phi_1(\mathbf{r}_1) & \phi_2(\mathbf{r}_1) & \dots & \phi_K(\mathbf{r}_1) \\ \phi_1(\mathbf{r}_2) & \phi_2(\mathbf{r}_2) & \dots & \phi_K(\mathbf{r}_2) \\ \dots & \dots & \dots & \dots \\ \phi_1(\mathbf{r}_N) & \phi_2(\mathbf{r}_N) & \dots & \phi_K(\mathbf{r}_N) \end{bmatrix}. \tag{9}$$

Fig. 2 shows the first three basis functions for the Atlantic Ocean, Indian Ocean, and Pacific Oceans. The first basis-function $\phi_1(\mathbf{x}_n)$ for all the three oceans shows a near-zonal structure. The second basis function $\phi_2(\mathbf{x}_n)$ shows a near-meridional structure for the Indian Ocean and Pacific Ocean and for the lower latitudes (30°N – 30°S) of the Atlantic Ocean. The third basis-function $\phi_3(\mathbf{x}_n)$ shows the east-west slanted dipole-pattern with opposite signs in northeastern and southwestern regions in the Indian Ocean and Pacific Ocean, and near-meridional structure in the North Atlantic and near-zonal structure in the South Atlantic. The higher order basis functions have more complicated variability structures.

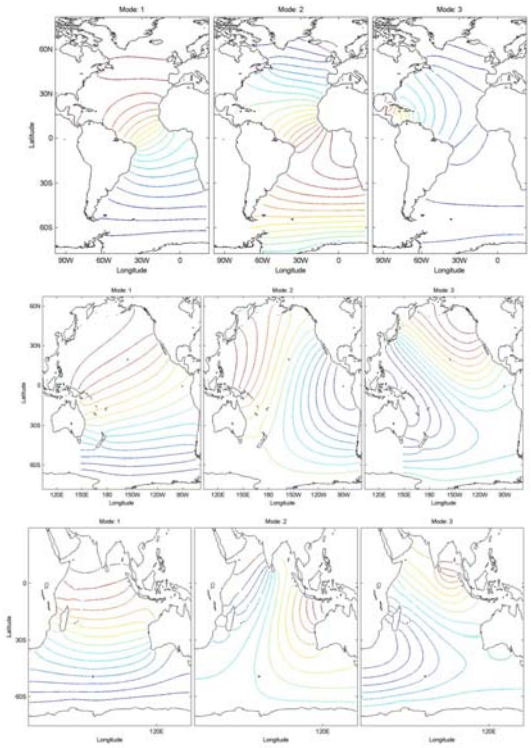

Fig. 2. First three basis functions for the (a) Atlantic Ocean, (b) Pacific Ocean, and (c) Indian Ocean [6].

In producing the SMG-WOD and SMG-GTSPP (T, S) data, around 30 basis functions are used. The OSD data assimilation equation is given by [10]

$$\mathbf{c}_a = \mathbf{c}_b + \mathbf{F}\mathbf{\Phi}^T \left[\mathbf{\Phi}\mathbf{F}\mathbf{\Phi}^T \right]^{-1} \mathbf{\Phi}\mathbf{H}^T\mathbf{d}, \tag{10}$$

where $\mathbf{F}$ is an $N \times N$ diagonal observational contribution matrix

$$\mathbf{F} = \begin{bmatrix} f_1 & 0 & 0 & 0 & 0 & 0 \\ 0 & f_2 & 0 & 0 & 0 & 0 \\ 0 & 0 & \ddots_i & 0 & 0 & 0 \\ 0 & 0 & 0 & f_n & 0 & 0 \\ 0 & 0 & 0 & 0 & \ddots & 0 \\ 0 & 0 & 0 & 0 & 0 & f_N \end{bmatrix}, \qquad f_n \equiv \sum_{m=1}^{M} h_{nm} . \tag{11}$$

The OSD method has been proven an effective ocean data analysis method. With it, several new ocean phenomena have been identified from observational data such as a bi-modal structure of chlorophyll-a with winter/spring (February–March) and fall (September–October) blooms in the Black Sea [11], fall–winter recurrence of current reversal from westward to eastward on the Texas–Louisiana continental shelf from the current-meter, near-surface drifting buoy [12], propagation of long Rossby waves at mid-depths (around 1000 m) in the tropical North Atlantic from the Argo float data [13], and temporal and spatial variability of global upper ocean heat content [3].

3. SMG (T, S) DATASETS

Six SMG (T, S, u, v) datasets have been produced using the OSD method and quality controlled by NOAA/NCEI scientists:

(1) Synoptic monthly gridded three dimensional (3D) World Ocean Database temperature and salinity from January 1945 to December 2014, **NOAA National Centers for Environmental Information** (NOAA/NCEI Accession 0140938) downloaded at https://data.nodc.noaa.gov/cgi-bin/iso?id=gov.noaa.nodc:0140938

(2) Synoptic Monthly Gridded WOD Absolute Geostrophic Velocity (SMG-WOD-V) (January 1945 - December 2014) with the P-Vector Method, **NOAA National Centers for Environmental Information** (NOAA/NCEI Accession 0146195) downloaded at https://data.nodc.noaa.gov/cgi-bin/iso?id=gov.noaa.nodc:0146195

(3) Synoptic monthly gridded Global Temperature and Salinity Profile Programme (GTSPP) water temperature and salinity from January 1990 to December 2009, **NOAA National Centers for Environmental Information** (NOAA/NCEI Accession 0138647) downloaded at https://data.nodc.noaa.gov/cgi-bin/iso?id=gov.noaa.nodc:0138647

(4) Synoptic monthly gridded (0.25°) three dimensional (3D) Mediterranean Sea (T, S, u, v) dataset (January 1960 - December 2013) from the NOAA/NCEI WOD Profile Data, **NOAA National Centers for Environmental Information** (NOAA/NCEI Accession 0157702), downloaded at https://data.nodc.noaa.gov/cgi-bin/iso?id=gov.noaa.nodc:0157702

(5) Synoptic monthly gridded (0.25°) three dimensional (3D) Japan/East Sea (T, S, u, v) dataset (January 1960 - December 2013) from the NOAA/NCEI WOD Profile Data, **NOAA National Centers for Environmental Information** (NCEI Accession 0157703), downloaded at https://data.nodc.noaa.gov/cgi-bin/iso?id=gov.noaa.nodc:0157703

(6) Synoptic monthly gridded (0.25°) Gulf of Mexico (T, S, u, v) dataset (January 1945 - December 2014) from the NOAA/NCEI WOD Profile Data, **NOAA National Centers for Environmental Information** (NOAA/NCEI Accession 0156423), downloaded at http://data.nodc.noaa.gov/cgi-bin/iso?id=gov.noaa.nodc:0156423

These datasets can be accessed openly from the NOAA/NCEI website. Among them, first three datasets are for the world oceans with the horizontal resolution of $1^o \times 1^o$, and the other datasets are for regional seas with the horizontal resolution of $0.25^o \times 0.25^o$. Table 1 shows the vertical depths of the datasets.

Table 1. Vertical depths of the SMG datasets.

Layer	Depth (m)	Layer	Depth (m)	Layer	Depth (m)
1	0	**11**	250	**21**	1200
2	10	**12**	300	**22**	1300
3	20	**13**	400	**23**	1400
4	30	**14**	500	**24**	1500
5	50	**15**	600	**25**	1750
6	75	**16**	700	**26**	2000
7	100	**17**	800	**27**	2500
8	125	**18**	900	**28**	3000
9	150	**19**	1000		
10	200	**20**	1100		

4. STUDY AREAS

Intra- and inter-annual (T, S) variability has been determined using the SMG data such as reported by Chu (2011). To identify its effect on high frequency acoustic propagation for regional seas with the Navy's interests, the South China Sea, Philippines Sea (Fig. 3a), Yellow Sea (Fig. 3b), and Mediterranean Sea (Fig. 3c) are selected for study. We use the SMG World Ocean Database to obtain intra- and inter-annual (T, S) variability, the High-Frequency Environmental Acoustics (HFEVA) data for bottom sediment, and DBDB-V for bathymetry. HFEVA and DBDB-V are obtained from the Naval Oceanographic Office (NAVOCEANO). The letters A, B, C, …, on the figures indicate the location for investigating the impact on acoustic propagation.

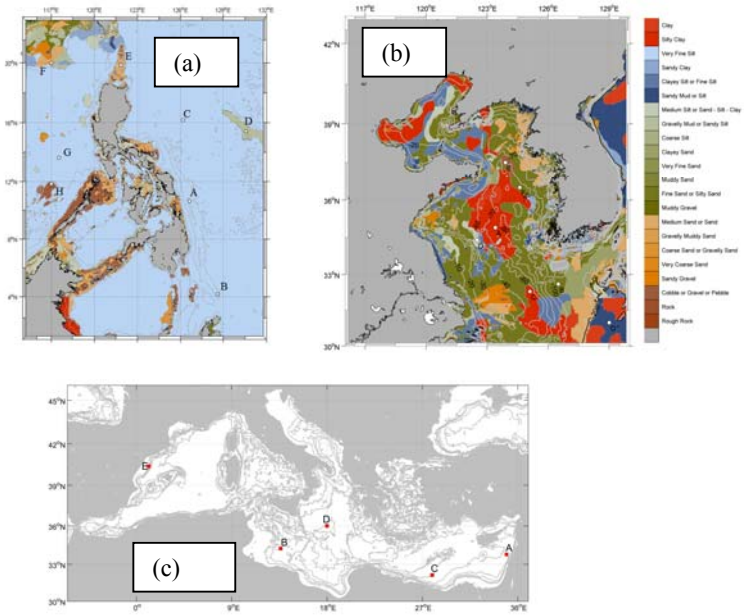

Fig. 3. Arears of interest: (a) South China Sea/Phillippine Seas [14], (b) Yellow Sea [15], and (c) Mediterranean Sea [16]. The letters A, B, C, …, on the figures indicate the location for investigating the impact on acoustic propagation.

5. INTER- AND INTRA-ANNUAL (T, S) VARIABILITY

Various SMG datasets depicted in Section 3 provide great opportunity to investigate inter- and intra-annual variability of (T, S) and in turn the sound speed profile (SSP). To assess the impact of the inter- and intra-annual variability on the acoustic propagation, temporally varying (T, S) profile data at selected location (Fig. 3) are extracted from SMG-WOD,

and then the SSP can be calculated. Fig. 4 shows temporal varying (T, S, SSP) profiles at the 5 locations in the Mediterranean Sea.

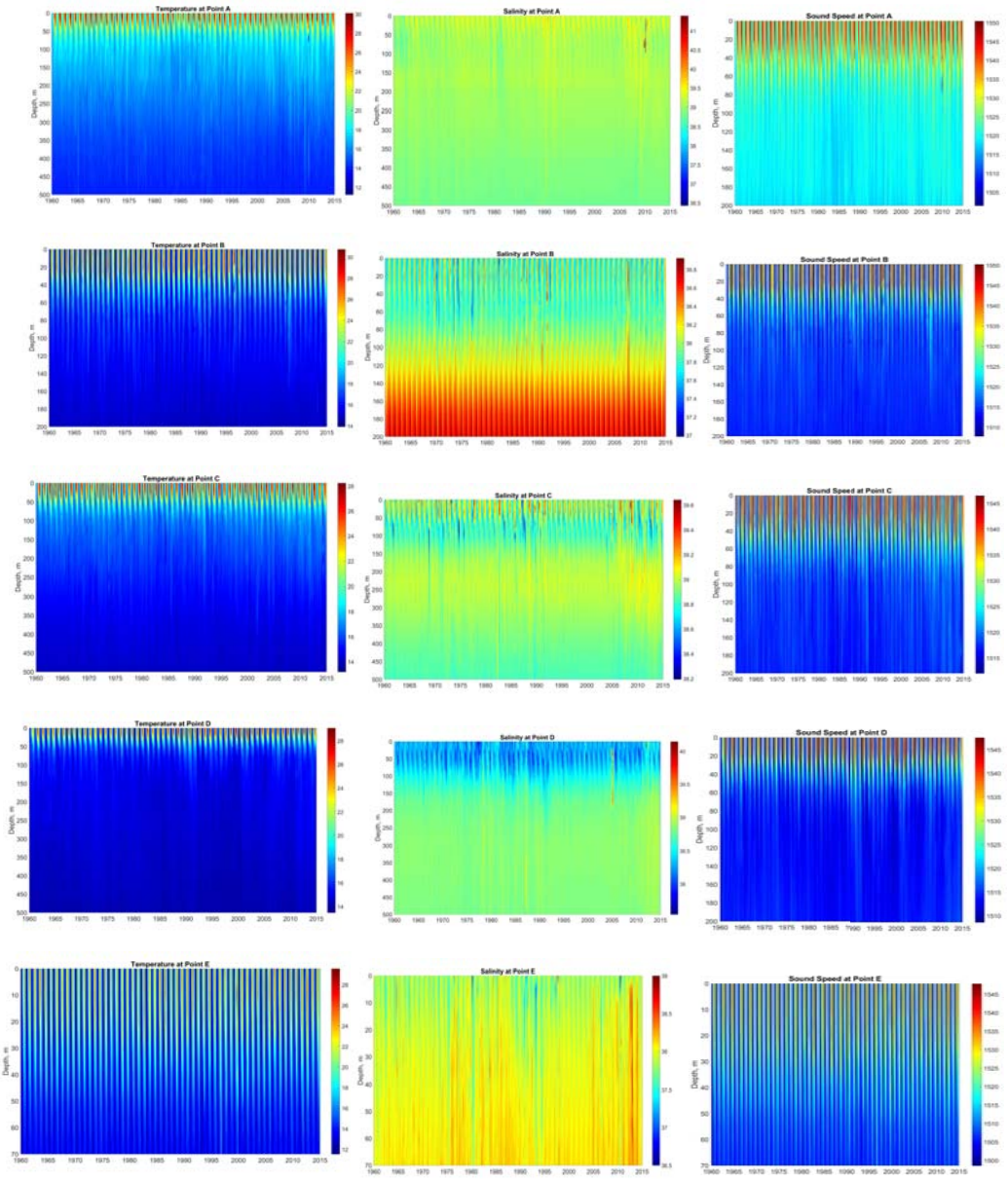

Fig. 4. Vertical and time cross sections of teperature (left panels), salinity (middle panels), and SSP (right panels) at 5 locations (A, B, C, D, E) in the Mediterranean Sea marked on Fig. 3c.

The temperature profiles at all the locations exhibit strong seasonal variation associated with surface heat fluxes and variations in the vertical structure of water column. However, the seasonality in the Mediterranean Sea (as an example) is strongly modulated by inter-annual and decadal variability (Fig. 4, left panels). For example, at location-A the inter-annual variability is evident in summer sea surface temperature, mixed layer depth, and strength of the thermocline. The temperature was colder between 1980 and 1990 at the surface and in the intermediate layer, with shallower summer

mixed layer observed in 1985-1986. The temperature increased between 1990 and 2014. Temperature between 1960 and 1980 was also warmer than 1980 to 1990, however, it was not warmer than period between 1990 and 2014. Strong variations of temperature with higher temperatures propagating down to 500 meters occurred in 2009-2010. At location-B, sea surface temperature was the warmest between 1997 and 1998 than other years. Also, warmer water between 2007 and 2008 extended down to 180 meters. At location-C the sea surface temperature exhibited a strong decadal variability especially between 2000 and 2014, the surface water gets warmer and this warmer water penetrated to deeper layers. An anomalously deep penetration of warm water down to 300 meters was observed during summer 1992. Interestingly, it was accompanied by colder than usual surface temperature and rather shallow mixed layer at the end of spring. Anomalously warm surface water but no deepening of the warm surface layer was observed during the summer 2012. At location-D (Fig. 4, left panels), a strong contrast existed in summer surface temperatures before and after 1980. The temperature at the surface started to increase after 1980. Before the 1980, the surface water is about 24 °C. Then it gets warmer at the surface and reaches 29 °C. Between 2000 and 2014 years, the warmer water starts to penetrate down to 400 meters. At location-E temperature increased between 1990 and 2014. The water between surface and a depth of 20 meters reached the higher temperature than previous years; however, the warmer water penetrated to deeper layer between 1997 and 1998. Sea surface temperatures between 1960 and 1990 were lower than later decades.

The salinity showed evident inter-annual variations at all locations (Fig. 4, middle panels). Overall, water became saltier from 1960 at location-A. The inter-annual and decadal variability at this location seems to be synchronized with the inter-annual variability of temperature. Specifically, the salinity increased between 1990 and 1995, and between 2008 and 2014. It did not increase between 1995 and 2008. Due to less saline Modified Atlantic Water at the surface, saltier water occurred below 80 m at location-B. The salty layer exhibited a very robust seasonality with an episodic increase in salinity in 2007. At the surface, there is high inter-annual variation in salinity; however, the salinity did not show steady increase between 1960 and 2014. The salinity decreased at the surface at some years between 1970 and 1990. These values were lower than values between 1960 and 1970. After 1990, the salinity increased, especially between 2007 and 2008. An apparent two-layer structure exists at location-D with fresher upper layer with depth of about 100 meters and saline water below. The two layers were separated by rather strong halocline. While some seasonality is evident in the upper layer, there were high inter-annual variations between surface 100-meter layer and the rest of the water column. The salinity at the surface decreased between 1980 and 1995. After 1995, the salinity started to increase. It reached its maximum value at 2007. The salinity increases in all layers between 2010 and 2014. The deep layer showed its highest inter-annual variations between 2010 and 2014. In 2005 an intrusion of salty water was seen in the subsurface layer between 30 and 200 meters. Evident inter-annual variability was identified in all depths at location-E. After 1975, the salinity started to increase until 1990. It decreased rapidly between 1990 and 1995. After the 1995, the salinity started to increase again at all levels. The salinity reached its maximum value between 2010 and 2014. Besides these long-term trends, occasional intrusions of anomalously fresh water in 1980, 1993 and 2011.

Comparison among (T, S, SSP) profiles (Fig. 4) shows that the SSP is more correlated with temperature profile than salinity profile as expected. The sound speed had evident seasonal variability at all locations. It had evident inter-annual variation below the mixed layer. For example, it had low values between 1980 and 1990, and high values between 2000 and 201440 m depth.at location-A, high values between 2007 and 2008 at location-B, high values in 1992 and between 2000 and 2014 and low values between 1980 and 1985 at location-C, decreased between 1980 and 2000 except 1990 and 1992 with low sound speeds at deeper layers and increased at all depths from 2000 to 2014 especially between 60 and 200 m at location-D, and lower sound speeds from 1960 to 1990 than from 2010 to 2014 at location-E.

6. SEDIMENT DATABASES AND GEOACOUSTIC PARAMETERS

There are four unclassified sediment databases: Enhanced, Standard, Reduced, and High Frequency Environmental Acoustics (HFEVA). The bottom sediment characteristics of the research area of interest can be extracted from any one of these databases, but with varying degrees of resolution available across the globe. “The Enhanced is the actual database that is maintained by NAVOCEANO. It is suitable for researchers and developers with technical geologic knowledge, or in cases where the most geologic information is desired” [17]. Due to the redundancy and sometimes

ambiguous nature of the large enhanced dataset, it is generally considered too cumbersome for operational application. Operational or tactical use of the data is best retrieved from a subset of the total data such as HFEVA (Table 2, used in the present research), reduced, or standard.

Table 2. HFEVA sediment categories [17].

HFEVA Standard Sediment Type	HFEVA Category
Rough Rock	1
Rock	2
Cobble or Gravel or Pebble	3
Sandy Gravel	4
Very Coarse Sand	5
Muddy Sandy Gravel	6
Coarse Sand or Gravelly Sand	7
Gravelly Muddy Sand	8
Medium Sand or Sand	9
Muddy Gravel	10
Fine Sand or Silty Sand	11
Muddy Sand	12
Very Fine Sand	13
Clayey Sand	14
Coarse Silt	15
Gravelly Mud or Sandy Silt	16
Medium Silt or Sand-Silt-Clay	17
Sandy Mud or Silt	18
Fine Silt or Clayey Silt	19
Sandy Clay	20
Very Fine Silt	21
Silty Clay	22
Clay	23
No data	*888*
Land	*999*

The HFEVA sediment categories are provided in Table 2. HFEVA categories range from 1–23, with two additional; 888 referring to "no data" and 999 referring to "land." The enhanced database includes 88 and 999, but the categories range from 0102–6890. The comparison between the HFEVA and the enhanced is that, grouping many similar bottom types under one category heading for simplification. For example, within the enhanced database code 3308 is listed as clay with the additional categorization as hemi-pelagic and terrigenous (HT). This corresponds to code 23 in the HFEVA database, which denotes a bottom type of clay. Depending on the field of study, it may be important to know that "pelagic and hemi-pelagic sediments are mostly fine-grained deposits, the product of slow deposition in typically low-energy depositional environments" which make up 50% of the Earth's surface (Garrison 1990). However, when the bottom type is composed of small particulate matter that responds acoustically similar regardless of the origin (land/sea, organic/inorganic) then less granularity of classification is required. Each sediment dataset for interested areas is plotted in order to determine which dataset is most appropriate for this research. The baseline resolution extracted was 1°. Individual sediment plots were also mapped at resolutions of 0.5° and 5.0° for comparison to the 1° resolution sediment data to see if there were significant differences necessitating resolutions other than 1°. The bottom type and bathymetry at selected locations (see Fig. 3) are presented in Table 3 for the Yellow Sea, Table 4 for the Philippine/South China Seas, and Table 5 for the Mediterranean Sea.

Table 3. Bottom sediment type and bathymetry at the selected locations in the Yellow Sea [15]

Location	Latitude °N, Longitude, °E	Depth (m)	Bottom Sediment Type
A	123.4, 34.9	70-80	silty clay
B	126.5, 32.6	>100	fine sand
C	125.1, 32.3	40-50	silty clay
D	122.5, 34.3	40-50	gravelly mud
E	123.9, 37.5	60-70	cobble or gravel
F	124.6, 36.5	70-80	fine sand
O	129.0, 31.0	>200	sandy mud

Table 4. Bottom sediment type and bathymetry at the selected locations in the Philippine/South China Seas [14]

Location	Latitude (N)	Longitude (E)	Depth (m)	Bottom Sediment
A	10.500	126.666	9000	Clay
B	4.2448	128.5458	6000	Clay
C	16.2204	126.2510	5000	Clay
D	15.4490	130.5917	5000	Coarse Silt
E	19.7956	121.7996	2000	Muddy Sandy Gravel
F	20.0	117.0	1500	Muddy Sandy Gravel
G	13.6293	117.6248	4000	Clay
H	11.8	117	300	Cobble or Gravel or Pebble

Table 5. Bottom sediment type and bathymetry at the selected locations in the Mediterranean Sea[16]

Location	Latitude (N)	Longitude (E)	Depth (m)	Bottom Sediment	Region
A	33.7794	34.939	1000	clay	Eastern
B	34.2399	13.6275	200	very fine sand	Central
C	32.1361	27.9229	1000	sandy mud	Eastern
D	36	18	1000	very fine silt	Eastern
E	40.3946	1,1739	70	sandy mud	Western

The geoacoustic parameters for the acoustic model vary based on the bottom type as determined from the sediment database. The pertinent geoacoustic parameters to this research are the attenuation coefficient and, the compressional sound speed, and the sediment density. The attenuation coefficient is calculated at each location (sediment type). The compressional sound speed (sound speed ratio) and the density are available in Table 6. From the sediment types listed in Tables 3-5, the geoacoustic parameters for the acoustic model can be determined.

Table 6. APL/UW TR9407 Geo-acoustic parameters associated with bulk grain size index used by acoustic model [17]

Bottom Sediment Composition	Bulk Grain Size Index	Long (32 Char) Name	Density gm/cm^3	Sound Speed Ratio	Wave Number Ratio
BOULDER	-9	Rough Rock	2.5	2.5	0.0137
ROCK	-7	Rock	2.5	2.5	0.0137
GRAVEL	-3	Gravel, Cobble or Pebble	2.5	1.8	0.0137
	-1	Sandy Gravel	2.492	1.337	0.01705
	-0.5	Very Coarse Sand	2.401	1.3067	0.01667
	0.0	Muddy Sandy Gravel	2.314	1.2778	0.01630
	0.5	Coarse Sand	2.231	1.2503	0.01638
	1.0	Gravelly Muddy Sand	2.151	1.2241	0.01645
SAND	1.5	Sand or Medium Sand	1.845	1.1782	0.01624
	2.0	Muddy Gravel	1.615	1.1396	0.01610
	2.5	Silty Sand or Fine Sand	1.451	1.1073	0.01602
	3.0	Muddy Sand	1.339	1.0800	0.01728
	3.5	Very Fine Sand	1.268	1.0568	0.01875
	4.0	Clayey Sand	1.224	1.0364	0.02019
	4.5	Coarse Silt	1.195	1.0179	0.02158
	5.0	Sandy Silt	1.169	0.9999	0.01261
	5.5	Medium Silt	1.149	0.9885	0.00676
SILT	6.0	Silt	1.149	0.9873	0.00386
	6.5	Fine Silt	1.148	0.9861	0.00306
MUD	7.0	Sandy Clay	1.147	0.9849	0.00242
	7.5	Very Fine Silt	1.147	0.9837	0.00194
	8.0	Silty Clay	1.146	0.9824	0.00163
CLAY	9.0	Clay	1.145	0.9800	0.00148
	10.0		1.145	0.9800	0.00148

7. ACOUSTIC RAY TRACING MODEL - BELLHOP

BELLHOP is an open source acoustic ray tracing model to predict acoustic pressure field in ocean environments and in turn transmission loss, eigenrays, arrivals, and received time-series[18]. Bellhop is designed in order to perform two-dimensional acoustic ray tracing for a given sound speed profile c(z) or a given sound speed field c(r, z), in ocean waveguides with at or variable absorbing boundaries." The bottom absorbing boundary is of particular interest in the research due the shallow water depths of the Yellow Sea. Modeling acoustic transmission with ray profiles is a common method for studying and understanding how sounds energy propagates within a given sound channel [18]. Dong et al. [19] confirmed strong agreement between BELLHOP and range- dependent acoustic model (RAM) developed at the Naval Research Laboratory (NRL) [20] after comparing model-predicted transmission loss. The sediment type translates into a bottom reflectivity coefficient. "To specify an arbitrary bottom reflection coefficient to characterize the bottom, then one must provide a bottom reflection coefficient file with angle-reflection pairs defining the reflectivity" [18]. Along with SSP profiles, they are environmental inputs into BELLHOP in order to produce a ray trace and further calculate transmission loss for ocean acoustics (Fig. 5). Transmission loss (TL) in decibels, dB, is calculated from the pressure field. While pressure in not a direct input parameter for BELLHOP it is generated from the depths input. The conversion for pressure, p, to dB is $20\log10(|p|)$. Transmission loss can be plotted in three different ways in BELLHOP. The user may select run criteria to plot transmission loss as coherent, incoherent, or semi-coherent depending on the desired detail of the acoustic field. Coherent transmission loss runs provided the most acoustic detail of the interferences patterns, but it also takes the longest to run. When such fine-patterned interference is not required, the user should select incoherent transmission loss, essentially an averaged transmission loss across a band of frequencies. Incoherent should not be used for deterministic forecasts. The third option, semi-coherent is essentially a combination of the previous two; it captures some but not all of the effects from interference.

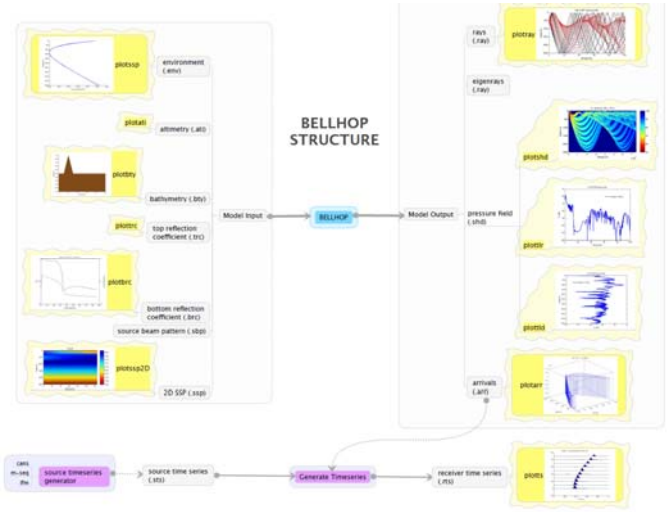

Fig. 5. Flow chart of BELLHOP: left panels show all the input sources that can be provided to BELLHOP. The right panels show all the model outputs [18].

8. ACOUSTIC PROPGATION RANGE

The desire to reduce submarine vulnerability resides in being able to detect submarines, particularly those that are ultra-quiet due to air independent propulsion (AIP). The Navy predominantly used mid-frequency sonar for prosecuting AIP diesel submarines; the mid-frequency range for this paper is considered to be 0.5 kHz to 5 kHz. The full extent of naval sonar capability extends beyond this mid-range, and the Navy will sometimes use specific systems that are of lower frequency for long-range detection, or higher frequencies as the tactical situation requires. Here, 3.5 kHz sound source is taken as an example for illustration. The sound source is placed at (8 m, 20 m) depths for the Yellow Sea, 40 m for the Mediterranean Sea, South China Sea, and Philippine Sea. For the Yellow Sea (shallow water with maximum water depth of 80 m), the sound frequency did not have a large impact on the TL when the sound source varying from 3.5 kHz to 0.5 kHz [15]. As determined from the SSP profiles, the greatest deviation from the total mean SSP profile occurred in August, and the least variation in January across all locations. TL was modeled for both SMG-WOD and GDEM at each location. The launching angle discretized with increment of 10^{o}, with varying combinations of source depth (SD) to receiver depth (RD). In order to quantify the propagation ranges to allow for comparison, several TL thresholds were used such as 60 dB, 70 dB, 80 dB, 90 dB, and 100 dB loss in order to analyze the difference in rates of TL across various locations in quantitative manner. The mean and maximum ranges with (SSP from SMG-WOD) and without interannual variability (SSP from GDEM) for all launching angles, and all source to receiver depths are listed for January (Tables 7–8) and August (Tables 9-10) for the Yellow Sea, which show large difference.

Table 7. January mean and maximum acoustic propagation ranges in the Yellow Sea with the SSP calculated from SMG-WOD[15].

Threshold (dB)	Range (km)	Location						
		A	B	C	D	E	F	O
60	mean	4.5142	4.4062	3.6771	5.0928	4.8623	3.6476	2.6214
	max	10.5967	9.9216	9.9216	11.4932	12.5317	11.4225	9.9216
70	mean	11.6788	12.2127	11.3663	12.9979	11.4653	9.1267	8.4181
	max	31.7003	31.1898	31.1898	32.9935	31.1898	31.1898	31.1898
80	mean	26.14.19	27.3951	25.1847	27.2414	25.2152	20.3387	18.0278
	max	53.9514	58.6182	54.7512	55.0608	53.9514	53.9514	53.9514
90	mean	47.6035	48.0953	43.9857	46.6375	41.9877	34.8001	31.4071
	max	87.9457	81.9004	84.5373	79.7884	77.0103	82.453	74.5893
100	mean	68.1388	69.7172	63.9175	68.2433	58.127	48.7102	44.9997
	max	92.3192	91.9653	91.9653	91.9653	91.9653	91.9653	91.9653

Table 8. January mean and maximum acoustic propagation ranges in the Yellow Sea with the SSP calculated from GDEM[15].

Threshold (dB)	Range (km)	Location						
		A	B	C	D	E	F	O
60	mean	3.2627	4.5386	2.8798	3.2001	6.7946	3.4232	1.413
	max	7.5583	7.9578	5.6569	5.5768	7.3418	4.4929	2.8922
70	mean	10.2989	11.2539	9.8557	10.4596	15.5678	9.0209	4.9732
	max	17.1218	16.4182	16.6187	17.6548	16.6254	11.0515	8.0957
80	mean	23.7641	22.8042	23.0009	28.6708	38.5399	18.2543	10.5838
	max	34.3483	32.9114	35.9501	46.157	39.379	23.4702	18.0085
90	mean	47.2287	43.7958	45.2065	46.0015	64.13	34.3497	20.968
	max	59.0338	57.6121	57.4838	61.5141	64.9756	42.3332	38.0115
100	mean	72.6501	63.1721	64.2717	60.2321	89.0296	54.3492	37.7323
	max	92.0613	74.2362	76.5833	73.0217	89.3854	63.7604	55.7593

Table 9. August mean and maximum acoustic propagation ranges in the Yellow Sea with the SSP calculated from SMG-WOD[15].

Threshold (dB)	Range (km)	Location						
		A	B	C	D	E	F	O
60	mean	1.457	3.5422	1.5666	2.2522	3.8924	2.6188	2.2326
	max	9.9216	9.9216	9.9216	9.9216	9.9216	9.9216	9.9216
70	mean	3.6554	7.9692	3.569	4.9789	9.4116	6.1479	6.0618
	max	31.1898	31.1898	31.1898	31.1898	31.1898	31.1898	31.1898
80	mean	7.7223	14.6942	7	9.9708	23.6079	11.7726	12.4431
	max	53.9514	53.9514	53.9514	53.9514	53.9514	53.9514	53.9514
90	mean	13.2845	24.4461	11.5323	16.3627	41.2092	19.0684	20.81
	max	74.5893	74.5893	74.5893	74.5893	74.5893	74.5893	74.5893
100	mean	18.9952	36.9348	15.1487	21.3142	58.0341	25.4549	29.4261
	max	91.9653	91.9653	91.9653	91.9653	91.9653	91.9653	91.9653

Table10. August mean and maximum acoustic propagation ranges in the Yellow Sea with the SSP calculated from GDEM [15].

Threshold (dB)	Range (km)	Location						
		A	B	C	D	E	F	O
60	mean	0.8339	2.8091	0.79208	1.427	5.4375	2.3219	0.84981
	max	0.98235	3.2964	0.96651	1.722	5.7659	2.6349	0.89771
70	mean	1.6139	6.106	1.3259	2.4962	11.7526	4.4197	3.4008
	max	2.0368	6.7257	1.5941	2.8337	12.1603	4.5578	3.4304
80	mean	2.671	10.2964	1.9617	4.1585	21.588	7.2814	6.8195
	max	3.1903	11.1137	2.1844	4.4257	23.7492	7.9183	6.8517
90	mean	3.7663	15.8272	2.6948	6.3945	37.4626	11.7533	12.3378
	max	4.2478	16.7245	2.8533	7.8383	43.1782	14.7736	12.3965
100	mean	4.8602	23.1134	3.5924	8.2717	59.7458	16.4812	23.5609
	max	5.358	25.1659	3.9414	10.2709	66.2201	21.7788	23.8398

9. CLIMATE IMPACT ON ACOUSTIC PROPAGATION

9.1. Range-time cross-section

Interannual variability of TL can be presented by range-time cross section for a given receiver depth (say 50 m). Fig. 6 shows such cross-sections for the 5 locations (A, B, C, D, E) in the Mediterranean Sea. At location-A, TL exhibits a high inter-annual variability mostly in all range. The highest TL at range longer than 10 km occurred between 1982 and 1990. Low TLs appeared at time periods from 1970 to 1982 and from 2010 to 2014. Conversely, Lower TLs were found during 1982 and 1990 than during 1970 and 1982 at close ranges (0–5 km). Location-B represents shallow water in the Central Mediterranean Sea. At this location, the main patterns of acoustic propagation are bottom bounce and surface duct. Interannual variability of TL is much weaker than at location-B than location-A. This may be caused by the shallow water and interactions with bottom. At location-C, TL changed quickly between 1960 and 1995. After 1995, the TL exhibited the same values. In addition, the TL appeared lower between 1995 and 2014. It may imply the increase of detection ranges after 1990. Since the thick horizontal contours of TL representing the convergence zone path, lower TL might occur at longer ranges due to the presence of caustics at the convergence zone. Three horizontal TL contours occurred at the same range over the all decades with weak interannual variability except ranges shorted than 38 km, where there were low TLs from 1960 to 1978, from 1985 to 1992, and from 2007 to 2014. Conversely, high TLs manifested from 1978 to 1985 and from 1992 to 2007, and low TLs occurred between 2007 and 2014.Three stripes of horizontal TL contours occurred at the same range over all decades at location-E with low interannual variability except ranges short than 38 km with the lowest TL occurred between 1967 and 1973.

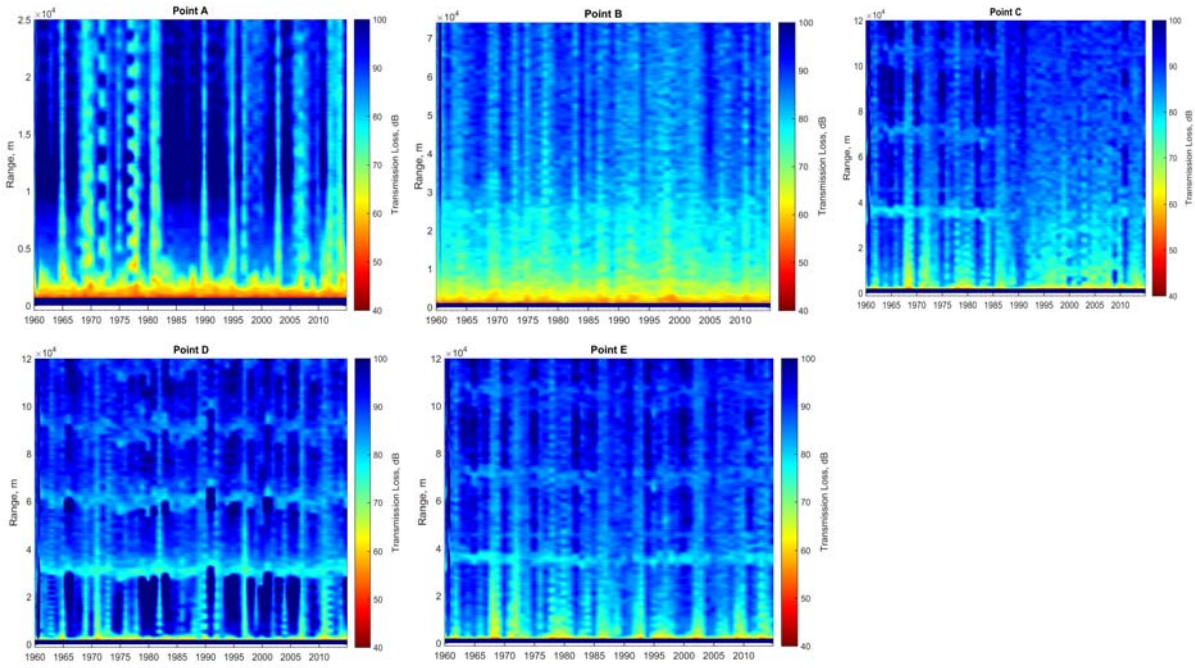

Fig. 6. Range-time cross sections of TL (unit: dB) with receiver at 50 m depth at locations A, B, C, D, and E in the Mediterranean Sea (marked on Fig. 3c). Horizontally oriented TL contours are evident in locations C, D, and F [16].

9.2. Depth-range cross section of ray paths and TL

Climate impact on acoustic propagation can be identified using SSP calculated from the SMG-WOD from different time periods in different seasons (January for winter and August for summer). The interannual variability is stronger in winter (January) than in summer (August). This asymmetry may be caused by mixes layer depth and sound-speed profile

because the Mediterranean Sea has very strong, severe winds in winter, but not in summer. Fig. 6 provides guide lines for selecting the time periods to show the effect of short-term climate change.

At location-A, three periods (1970-1979, 19080-1990, 2000-2014) were chosen. Interannual variability of TL is weaker in summer (August) than in winter (January) (Fig. 7). A striking feature in January is the low TL at the surface duct with the upper ray limit of the convergence zone. This low TL zone has strong interannual variability with low TL (~65 dB) during 1970-1979), increased TL (~80 dB) during 1980-1990, and reduced TL (~65 dB) during 2000-2014. At close range (less than 3 km), TL for the whole depth was around 60 dB during 1970-1979, 50 dB during 1980-1990, and 60 dB during 2000-2014. Higher TL during 1970-1979and 2000-2014 than during 1980-1990 was also found at long ranges.

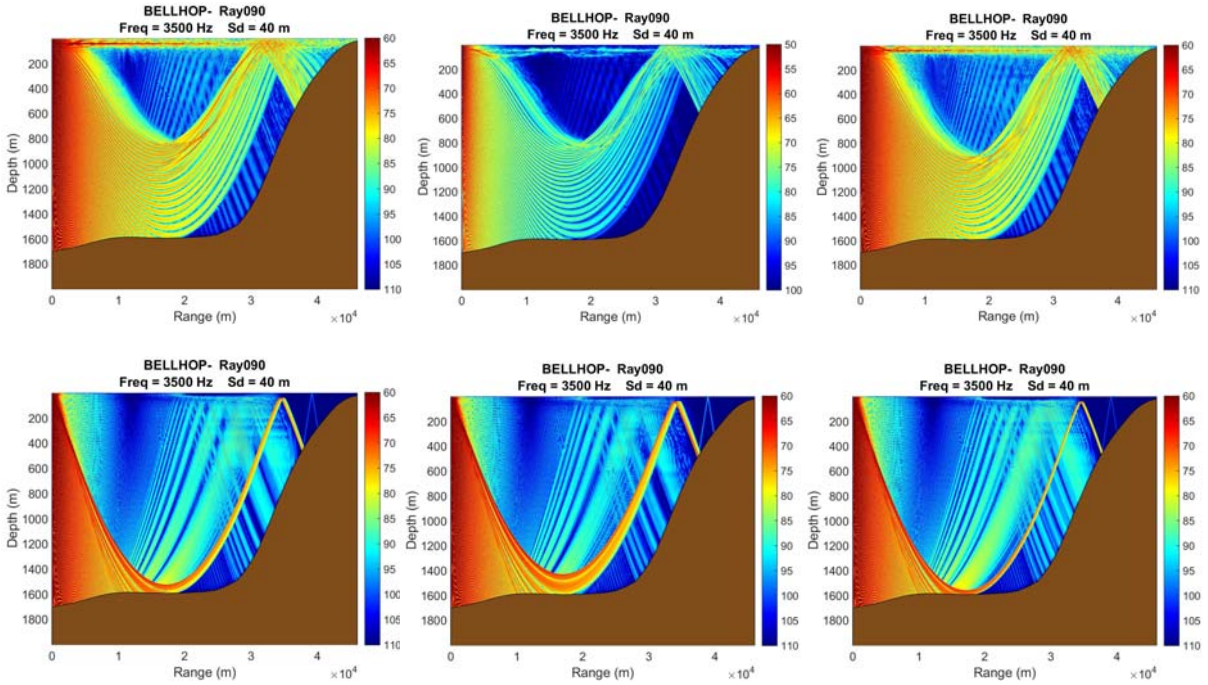

Fig. 7. Climate impact on the ray paths and TL (unit: dB) at location-A in the Mediterranean Sea (marked on Fig. 3c) with the source depth at 40 m indentified from three time periods: 1970-1979 (left panels), 1980-1990 (middle panels), and 2000-2014 (right panels) for January (upper panels) and August (lower panels) [16].

At location-B (Fig. 8) in January, the surface duct weakened and bottom bounce strengthened during 1997-1998 (upper left panel) and 2007-2008 (upper middle panel), as compared to the multi-year average (upper right panel). In August, the bottom bounce weakens and changes into a surface sound channel during 1997-1998 (lower right panel), lower TL at longer ranges during 2007-2008 (lower middle panel) with a higher TL occurring at all ranges.

At location-C (Fig. 9), two time periods were selected to show the climate impact: 1980–1995 and 2000–2014. In January, the TL showed convergence propagation and upper limiting ray of the convergence zone that extends to a depth of 800–1000 m depth during 1980-1995, and 900-1100 m during 2000-2014. In August, the TL had convergence zone propagation in both the time periods. However, there was slight difference between the upper limiting rays of the convergence zone. The upper limiting ray extends to a depth of 1500 meters in 1980-1995 and a depth of 1600 meters in 2000-2014.

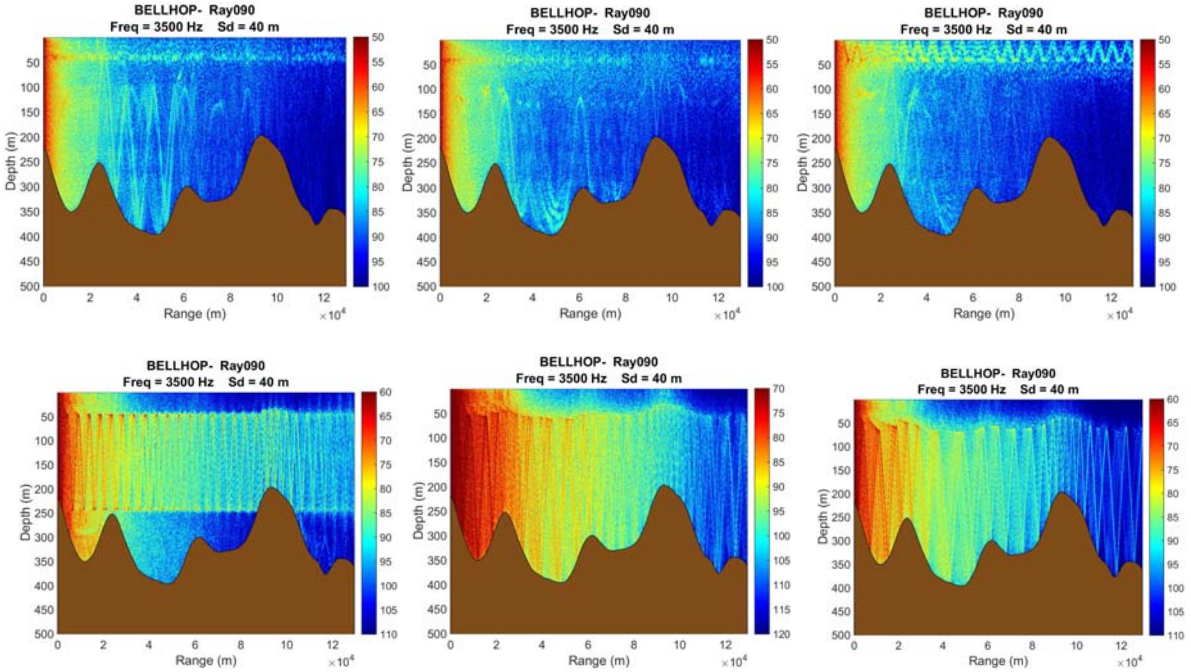

Fig. 8. Climate impact on the ray paths and TL (unit: dB) at location-B in the Mediterranean Sea (marked on Fig. 3c) with the source depth at 40 m indentified from three time periods: 1997-1998 (left panels), 2007-2008 (middle panels), and multi-year (1960-2014) monthly average (right panels) for January (upper panels) and August (lower panels) [16].

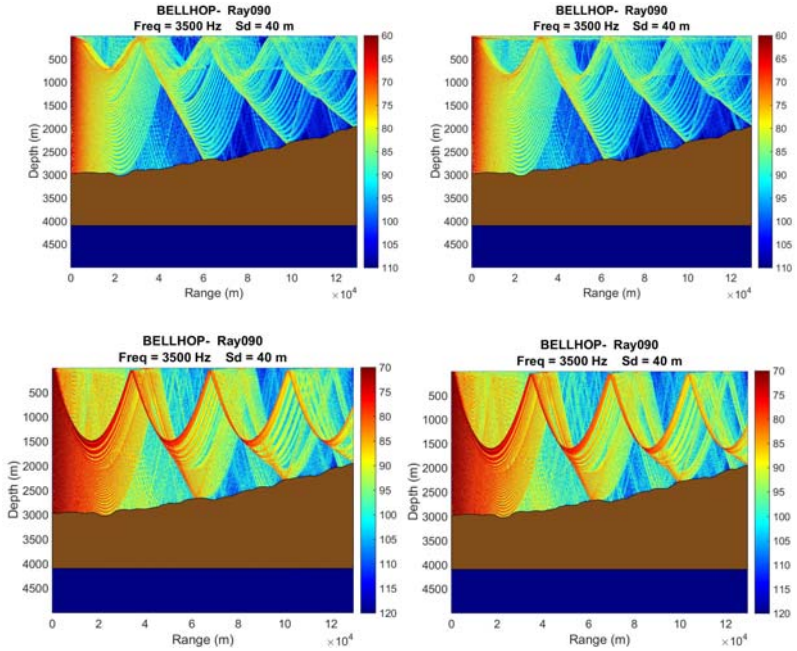

Fig. 9. Climate impact on the ray paths and TL (unit: dB) at location-C in the Mediterranean Sea (marked on Fig. 3c) with the source depth at 40 m indentified from three time periods: 1980-1995 (left panels), and 2000-2014 (right panels) for January (upper panels) and August (lower panels) [16].

At location-D (Fig. 10), two time periods were selected to show the climate impact: 1990-2000, 2000-2014. In January, the ray paths had evident inter-annual variability in the shadow zones near the surface. In August, both time periods demonstrate almost the same sound propagation pattern and TL. However, slightly lower TL was identified at long ranges during 1990-2000 than during 2000-2014.

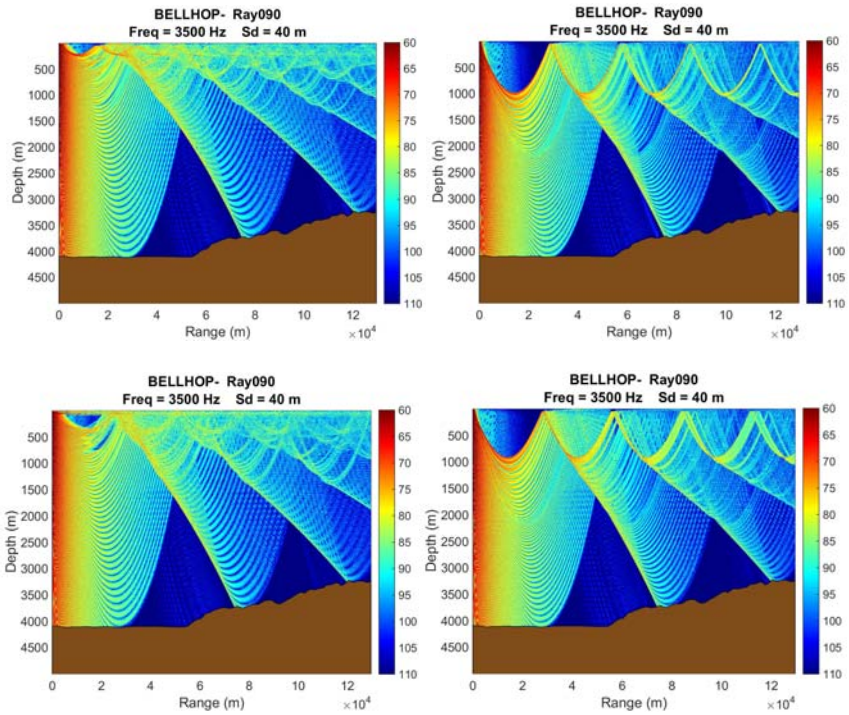

Fig. 10. Climate impact on the ray paths and TL (unit: dB) at location-D in the Mediterranean Sea (marked on Fig. 3c) with the source depth at 40 m indentified from three time periods: 1980-1995 (left panels), and 2000-2014 (right panels) for January (upper panels) and August (lower panels) [16].

At location-E (Fig. 11), two time periods were selected to show the climate impact: 1960-1970, and from 2000- 2014 with high and similar interannual variability in both winter (January) and summer (August). During 1960-1970, a low TL zone occurred near the surface with long range and vertically concentrated propagation between the surface and 300 m depth. During 2000-2014, a sound channel was identified with surface propagation together with higher TLs at long ranges and a lower TLs at short ranges comparing to the earlier period (1960-1970). Furthermore, the sound propagated to deeper layer during 1960-1970 than during 2000-2014.

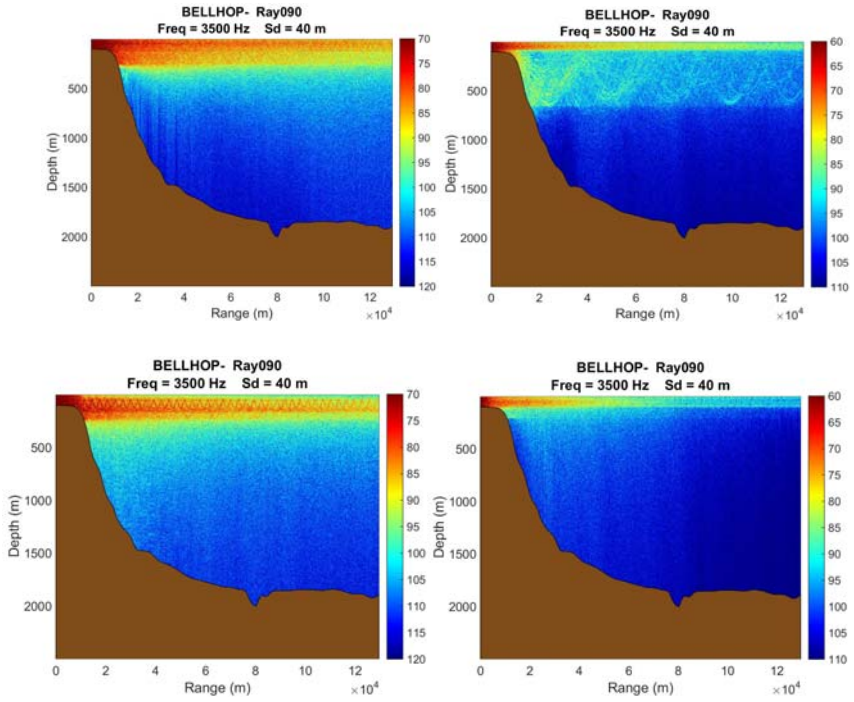

Fig. 11. Climate impact on the ray paths and TL (unit: dB) at location-E in the Mediterranean Sea (marked on Fig. 3c) with the source depth at 40 m indentified from three time periods: 1980-1995 (left panels), and 2000-2014 (right panels) for January (upper panels) and August (lower panels) [16] .

10. CONCLUSIONS

This study identifies the effects of intra- and inter-annual ocean environmental variability on the acoustic propagation in several regional seas such as the Mediterranean Sea, Philippine Sea, and South China, and Yellow Sea using the recently established synoptic monthly gridded (SMG) (T, S) data and an open source acoustic ray tracing model (BELLHOP). These effects vary with the location and time period. The overall average TL ranges between the two datasets same, but because SMG-WOD data contains intra- and inter-annual variability, several extended ranges were found for acoustic transmission that break out well past the GDEM TL ranges, not by a mere one or two km but in some cases twice the average TL range such that 20km detection range may jump to 40 km depending in the environment at the time.

This research also reveals the sensitivity of BELLHOP; it is sensitive enough to produce different TL results based on the variations of source and receiver depths when given the same SSP input. BELLHOP is also sensitive to the attenuation values for the bottom sediment, as location E in the Yellow Sea had the hardest, most reflective bottom type and the in both datasets it modeled the longest ranges as opposed to most of the other locations being silty clay or mud and BELHHOP modeled significantly shorter ranges.

For a general study, either database (SMG-WOD or GDEM) would be relevant because the average TL ranges are very close, but for tactical naval application, this research shows that in shallow water, the TL range variations between the two datasets can be significant. Just a few km extension of TL range can greatly increase the entire ensonification coverage area, which is crucial for sonar operators on submarines or ships, or of unmanned. This research shows that TL ranges may vary up to 10km or further, depending on the combination of source depth to receiver depth, which is important since submarines are not fixed in a vertical position. As the submarine varies its depth, it can greatly affect its detection vulnerability, or based on the season, it may choose to avoid an entire shallow operating area where ranges are poor.

This research is very specific to the Mediterranean Sea, Philippine Sea, and South China, and Yellow Sea Yellow Sea, as it such a shallow body of water, and while it may produce results comparable to other shallow bodies of water such as the Arabian Gulf, it would provide greater insight to actually conduct this same study but in multiple other ocean. For deeper oceans, the resolution differences between the datasets may not impact the results, and the SSPs will have different structures as no correlation was found between the SSP variability and any published indices, a beneficial future area of research would be to pair an oceanographic study of acoustic variability with a meteorological study to develop and test various EAMIs and the search for a correlation to acoustics. It would also be valuable to expand upon this research by comparing in situ TL data ranges to the projection of SMG-WOD and GDEM ranges in order to see how the real world matches up to the models.

ACKNOWLEDGMENTS

This research was sponsored by OPNAV-N2N6E (topic sponsor: CAPT Chris Gabriel) and OPNAV-N97 (topic sponsor: Dr. Andrew Greene) through NPS Naval Research Program.

REFERENCES

[1] Chu, P.C., "Observational studies on association between eastward equatorial jet and Indian Ocean dipole," J. Oceanogr., 66, 429-434 (2010).
[2] Weng, H., Ashok, S. K., Behera, S., Rao, A., and Yamagata, T., "Impacts of recent El Nino Modoki on dry/wet conditions in the Pacific rim during boreal summer," Clim. Dyn, DOI 10.1007/s00382-007-0234-0 (2007).
[3] Chu, P.C., "Global upper ocean heat content and climate variability," Ocean Dyn., **61**, 1189-1204 (2011).
[4] Phillips, H. E., and Wijffels, S. E., "Interannual variability in the freshwater content of the Indonesian-Australian Basin," Geophys. Res. Lett., 32, L03603, doi: 10.1029/2004GL021755 (2005).
[5] Boyer, T., Levitus, S., Garcia, H., Locarnini, R.A., Stephens, C., and Antonov, J., "Objective analysis of annual, seasonal, and monthly temperature and salinity for world ocean on a 0.25^{o} grid," Int. J. Climatol., 25, 931-945 (2005).
[6] Chu, P.C., and Fan, C.W., "Synoptic monthly gridded global and regional four dimensional WOD and GTSPP (T, S, u, v) fields with the optimal spectral decomposition (OSD) and P-vector methods," Geosci. Data J., submitted.
[7] Chu, P. C., Ivanov, L. M., Korzhova, T. P., Margolina, T. M., and Melnichenko, O. M., "Analysis of sparse and noisy ocean current data using flow decomposition. Part 1: Theory," J. Atmos. Oceanic Technol., 20, 478-491 (2003a).
[8] Chu, P. C., Ivanov, L. M., Korzhova, T. P., Margolina, T. M., and Melnichenko, O. M., "Analysis of sparse and noisy ocean current data using flow decomposition. Part 2: Application to Eulerian and Lagrangian data," J. Atmos. Oceanic Technol., 20, 492-512 (2003b)
[9] Chu, P.C., Tokmakian, R.T. , Fan, C.W., and Sun, C.L., "Optimal spectral decomposition (OSD) for ocean data assimilation," J. Atmos. Oceanic Technol., 32, 828-841 (2015).
[10] Chu, P.C., Fan, C.W., and Margolina, T., "Ocean spectral data assimilation without background error covariance matrix," *Ocean Dyn.*, 66: 1143-1163, DOI 10.1007/s10236-016-0971-x (2016).
[11] Chu, P.C., Ivanov, L.M. and Margolina, T.M., "Seasonal variability of the Black Sea Chlorophyll-a concentration," *J.* Mar *Syst*, 56, 243-261 (2005).
[12] Chu, P.C., Ivanov, L.M. and Melnichenko, O.M., "Fall-winter current reversals on the Texas-Louisiana continental shelf," J. Phys. Oceanogr., 35, 902-910 (2005).
[13] Chu, P.C., Ivanov, L.M., Melnichenko, O.V. , and Wells, N.C., "Long baroclinic Rossby waves in the tropical North Atlantic observed from profiling floats," J. Geophys. Res., 112, C05032, doi:10.1029/2006JC003698 (2007).
[14] Judono, A.M., , "Inter-annual Variability of the Acoustic Propagation in the Philippine Sea Identified from a Synoptic Monthly Gridded Database as Compared with GDEM," MS Thesis on Meteorology and Oceanography, Naval Postgraduate School, June 2017
[15] McDonald, C.M, "Inter-annual Variability of the Acoustic Propagation in the Yellow Sea Identified from a Synoptic Monthly Gridded Database as Compared with GDEM," MS Thesis on Meteorology and Oceanography, Naval Postgraduate School, September, 2006.
[16] Kucukosmanoglu, M., "Inter-annual Variability of the Acoustic Propagation in the Mediterranean Sea Identified from a Synoptic Monthly Gridded Database as Compared with GDEM," MS Thesis on Meteorology and Oceanography, Naval Postgraduate School, December, 2006.

[17] Naval Oceanographic Office, "Database description for bottom sediment type Digital Bathymetric Data Base–Variable Resolution (DBDB-V) Version 5.4 (U)," Oceanographic and Atmospheric Master Library., OAML-DBD-90, 55 pp. (2006).
[18] Porter, M. B, "The BELLHOP Manual and User's Guide: PRELIMARY DRAFT," Heat, Light, and Sound Research, Inc. 57 pp (2011)
[19] Dong, L., Dong, H. and Hovem, J., 'Bellhop – a modelling approach to sound propagation in the ocean'. Submitted to Proceedings for the 37th Scandinavian Symposium on Physical Acoustics. [Available online at https://www.ntnu.edu/documents/14687435/901262351/SSPA_2014_Dong_Bellhop.pdf/9e4d79dc-1c5a-43d0-9724-9990bd5e2219] (2014).
[20] Zingarelli, R.A., and King, D.B., "RAM to Navy standard parabolic equation: transition from research to fleet acoustic model," NRL [Available online at http://www.nrl.navy.mil/research/nrl-review/2003/simulation-computing-modeling/zingarelli/] (2003).